Soft Matter

PAPER

View Article Online
View Journal

Cite this: DOI: 10.1039/d2sm01403c

Mapping hyperbolic order in curved materials†

Martin Cramer Pedersen, *[a] Stephen T. Hyde, [b] Stuart Ramsden[c] and Jacob J. K. Kirkensgaard [ad]

Received 25th October 2022,
Accepted 23rd January 2023

DOI: 10.1039/d2sm01403c

rsc.li/soft-matter-journal

Nature employs an impressive range of topologically complex ordered nanostructures that occur in various forms in both natural and synthetic materials. A particular class of these exhibits negative curvature and forms periodic saddle-shaped surfaces in three dimensions. Unlike pattern formation on flat or positively curved surfaces like spherical systems, the understanding of patterning on such surfaces is highly complicated due to the structures being intrinsically intertwined in three dimensions. We present a new method for visualisation and analysis of patterns on triply periodic negatively curved surfaces by mapping to two-dimensional hyperbolic space analogous to spherical projections in cartography thus effectively creating a more accessible "hyperbolic map" of the pattern. Specifically, we exemplify the method *via* the simplest triply periodic minimal surfaces: the Primitive, Diamond, and Gyroid in their universal cover along with decorations from a soft materials, whose structures involve decorations of soft matter on negatively curved surfaces, not necessarily minimal.

Introduction

The role of curvature in material science has a long history, going back at least a century to J. J. Thompson and his study of charge distributions on a sphere[1] which in recent times has found relevance in a range of spherical packing problems from viral capsid patterning,[2] colloidosomes,[3] superconducting films,[4] polymer self-assembly[5] and many other examples related to spherical defect distributions.[6] Packings on spheres constitute phenomena related to surfaces with positive Gaussian curvature, but more recently related problems on negatively-curved surfaces have been explored both theoretically and experimentally.[7–11] These studies have focused on patterning on a catenoid, one of the simplest examples of a negatively-curved and embedded (*i.e.* not self-intersecting) minimal surface. Another important class of negatively curved surfaces are triply-periodic hyperbolic surfaces which underly an extraordinary variety of assemblies in materials. The simplest examples, which have zero mean curvature are the triply-periodic minimal surfaces (TPMS). In particular, the topologically simplest and most symmetric TPMS, the Primitive surface,[12] Diamond surface[12] and Gyroid surface[13] all shown in Fig. 1(a) are related to the microstructures of many materials, both actual and hypothetical, perhaps best known from soft materials as bicontinuous phases routinely observed in block copolymer melts[14] and lipid-based lyotropic liquid crystalline systems.[15]

Our approach is applicable to any bicontinuous film, which generates a pair of interwoven three-periodic labyrinths, without self-intersections. The most symmetric examples are the Primitive, Diamond, and Gyroid TPMS as just mentioned, and in the case of lyotropic liquid crystals, there is good evidence that self-assembled bilayers lie on TPMS,[18–21] although we note that the physical interfaces are displaced to either side of the TPMS. More generally, microstructural interfaces in a range of materials are topologically equivalent to these TPMS, but may not have vanishing mean curvature, characteristic of minimal surfaces. However, they are triply-periodic, with the same underlying lattices and topology as the TPMS. For convenience, we call all such surfaces TP(M)S; these are defined more carefully in the ESI.† These TP(M)S appear at many different length scales in condensed materials and in the natural world. They are responsible for structural coloring in butterfly and other insect species, due to the TP(M)S ultrastructure of the chitin matrix in their external scales, which acts as a photonic crystal.[22] Similar structures are found within sub-cellular organelles: so-called cubic membranes have been identified in all kingdoms of life,[23] including photosynthetic chloroplast-precursors of higher plants or spatially complex bicontinuous lipid phases in lung surfactants.[15] They are also hypothesized to exist at sub-nuclear length scales in nuclear pasta – generated under conditions typical of a supernova explosion.[24] At less exotic conditions, negatively-curved graphitic carbon ("schwarzites"), whose covalent network describes a tessellation

[a] Niels Bohr Institute, University of Copenhagen, Denmark. E-mail: mcpe@nbi.ku.dk
[b] School of Chemistry, University of Sydney, Australia
[c] National Computational Infrastructure (NCI) Vizlab, Australian National University, Australia
[d] Department of Food Science, University of Copenhagen, Denmark

† Electronic supplementary information (ESI) available. See DOI: https://doi.org/10.1039/d2sm01403c

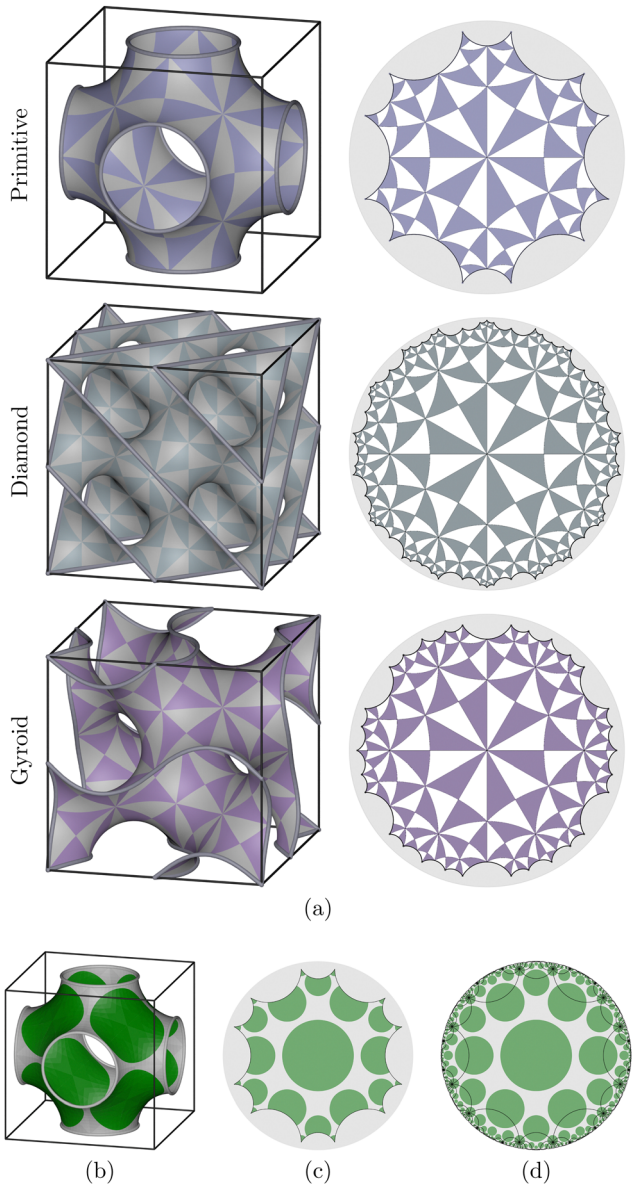

Fig. 1 (a) Left column: Orthographic visualizations of the three TPMS in their conventional cubic unit cells. Right column: These unit cells shown in the Poincaré disc model of $\mathbb{H}^2$.[16,17] These contain 96, 384, and 192 triangles, respectively. The space groups describing the symmetries of the embeddings in the left column are $Pm\bar{3}m$, $Fd\bar{3}m$, and $I4_132$; and each triangle in the images on the right is a domain of the symmetry group labeled *246. (b) A decorated unit cell of the Primitive surface. (c) A hyperbolic dodecagon representing a single copy of the unit cell domain of the Primitive surface shown in (b) drawn in the universal covering space, $\mathbb{H}^2$. (d) Multiple (in fact infinite) copies of the unit cell generated by translating the patch in (c) by a six-dimensional lattice, comprised of the three translational symmetries of the surface and three in-surface collars (here, these collars are defined by the loops on the faces of the bounding cube).

of TPMS structures analogous to the tilings of positively-curved surfaces of fullerenes, have been recently synthesised.[25] The negative-curvature and resulting complex topology of schwarzites imposes topological constraints on allowed atomic rings in the structure:[26] those constraints are likely responsible for paramagnetism in related graphitic materials,[27,28] for example. More recently, novel hard materials incorporating TPMS structures (*via* soft intermediates) have been successfully synthesised, with significant potential to tailor exotic collective magnetic and superconducting properties, specific to their negative curvature.[29,30] Evidently, these convoluted structures are relevant to an extraordinary variety of natural and synthetic materials.

A complex feature of all TP(M)S is their intrinsic two-dimensional geometry: they are, on average, hyperbolic (*i.e.* saddle-shaped, with negative Gaussian curvature). The simplest members, TPMS, are in fact hyperbolic everywhere on the surface, except at isolated points, although their curvature varies symmetrically over the surface. In contrast, hyperbolic two-space, $\mathbb{H}^2$, has negative and constant Gaussian curvature. A crucial observation is that $\mathbb{H}^2$ is a covering space of the TPMS in Fig. 1.[31] Similarly, it covers all TP(M)S. This implies that many symmetric patterns in $\mathbb{H}^2$ can be mapped to crystalline patterns in three-dimensional euclidean space ($\mathbb{E}^3$) as follows. First, decorate $\mathbb{H}^2$, then map that pattern onto a TP(M)S. That has been done for TPMS. The final crystalline patterns are realised by embedding those decorated TPMS in $\mathbb{E}^3$, then removing the TPMS substrate, leaving the decoration in $\mathbb{E}^3$. In short, the process proceeds from (curved) two-dimensions to (flat) three-dimensional space. That pathway is computationally convenient, allowing pattern enumeration *ab initio* in two-dimensions rather than three. For example, tessellations of $\mathbb{H}^2$ can be realised by a broad variety of finite tiles, whose edges induce crystalline networks, of relevance to chemistry, physics, and mathematics.[32–41] Further, tessellations of $\mathbb{H}^2$ by infinite ribbon-shaped tiles, related to so-called "free tilings"[34,35,42,43] map to complex interwoven networks in $\mathbb{E}^3$ *via* TPMS, which match patterns found in numerical simulations of self-assembled star polymers.[42,44,45] The latter will be reconsidered later in this paper.

Here, we present a computational solution to the inverse problem, allowing us to map from a topologically complex structure in conventional three-dimensional space ($\mathbb{E}^3$), either confined to a TPMS or a more generic hyperbolic, three-periodic surface, a TP(M)S, or forming a film resembling a thickened TP(M)S, onto a two-dimensional diagram on the flat page, which captures essential geometric features of the original surface structure. In principle, any hyperbolic surface can be mapped as described below. Our procedure is loosely analogous to the problem of exploring geography of the terrestrial globe *via* a flat map; however, our globe is a TP(M)S, with endless interwoven labyrinths. In essence, our procedure unfolds a patterned TP(M)S forming a pattern on $\mathbb{H}^2$, which in turn is mapped onto the flat page. Most importantly, the procedure affords a simple "quasiconformal" metric distortion of the original pattern which is readily identified, allowing the intrinsic in-surface symmetries of the patterned TP(M)S to be explored within the flat map. The technique allows unprecedented quantitative structural analysis of hyperbolic two-dimensional patterns, from ideal crystals to disordered "melts" as we will demonstrate *via* examples below.

The paper is structured as follows. First, we describe the relationship of the simplest (and most symmetric) hyperbolic surfaces embedded in $\mathbb{E}^3$, the Primitive, Diamond and Gyroid TPMS, to the hyperbolic plane and describe our algorithm to transform discretised meshes of TPMS into a flat mesh confined to the unit disc. We then explore the nature of intrinsic order in hyperbolic surfaces, classified *via* two-dimensional orbifold symbols (described in detail in the ESI† and elsewhere[46,47]) and demonstrate the retention of that order in a discretised flat disc map, modulo the metric rescaling required to map from TPMS (or TP(M)S) onto the disc *via* the hyperbolic plane. Lastly, we present a number of applications of our algorithm to very different materials with varying degrees of hyperbolic order, from hard discs to copolymeric assemblies.

Curvature and hyperbolic surfaces

We focus first on the three TPMS in Fig. 1(a) since they are the archetypal representatives of the broad class of related surfaces, TP(M)S, whose interfaces are, like TPMS, three-periodic and hyperbolic. We summarise the mathematical features of curved (minimal) surfaces, including TPMS and TP(M)S, in the ESI.† Throughout the manuscript, we shall distinguish between ''intrinsic'' properties of these surfaces, which are independent of the manner in which these surfaces are embedded in the ambient space, and ''extrinsic'' properties which depend on embedding. We note that in fact, among all TP(M)S, TPMS are maximally intrinsically symmetric in $\mathbb{E}^3$, and the most intrinsically symmetric are the Primitive, Gyroid and Diamond surfaces.[48] All three are related to each other by the Bonnet transformation[13,49,50] so they are intrinsically identical and can therefore be superimposed on each other (with suitable cuts), with identical curvature and metric variations over the surface. However, their extrinsic embeddings are different: the same hyperbolic surface admits three different embeddings in $\mathbb{E}^3$, forming different arrangements of channels (labyrinths) on either side of the TPMS, surrounded by ''collars'' on the TPMS. As a result, the three TPMS have distinct cubic space groups, listed in Fig. 1(a). We note in passing that the Gyroid admits two embeddings in $\mathbb{E}^3$ whose differences only emerge when the surface is decorated by a pattern which is intrinsically chiral (*i.e.* without in-surface reflection symmetry).[51]

The translational periodicity and non-trivial topology (induced by the collars) of these TPMS give rise to two ways of visualizing a specific pattern: (i) each distinct point on the TPMS as well as all of its copies by some translation vector in $\mathbb{E}^3$, maps to a distinct image point in $\mathbb{H}^2$, giving a finite patch in $\mathbb{H}^2$ corresponding to a single unit translational domain (a unit cell) of the surface, and (ii) each point in a single unit cell maps to multiple distinct points in $\mathbb{H}^2$ covering $\mathbb{H}^2$ completely.

Of particular importance to us is the notion of the universal cover of a surface; which is defined as a space in which each point corresponds (not necessarily one-to-one) to a point on the surface, and in which all closed curves can be contracted to a single point (*i.e.* the universal cover is ''simply connected''). Our goal is to map patterns on these three TP(M)S onto the flat page, conserving symmetries as far as possible as well as structural contiguity (so that adjacent elements remain adjacent). Since all TP(M)S have variable Gaussian curvature and their universal covers ($\mathbb{H}^2$) do not, it is impossible to map them onto $\mathbb{H}^2$ without some distortion of lengths (just as the Earth cannot be mapped onto the page without distortion). However, a discretised map, which preserves angles to an arbitrary accuracy dependent on the discretisation grid, is possible. Further, any symmetry in the TP(M)S can be mapped to a symmetry in $\mathbb{H}^2$, which is then identifiable on the flat page by a further step. Hyperbolic space is – to say the least – extensive. (For example, the tiling in Fig. 1(d) describes an infinite number of copies of the complete Primitive surface, which includes an unbounded number of copies of the unit cell, translated in all three directions.) Remarkably, it can be squeezed into an open unit disc on the flat page *via* the Poincaré (disc) model of $\mathbb{H}^2$ (described in the ESI†).

In technical terms, we seek a conformal map from our TP(M)S in $\mathbb{E}^3$ to their universal cover, $\mathbb{H}^2$. Many such maps are suitable; examples include the Gauss map,[52] the Schwarz–Christoffel map[53] and Stephenson's circle packing algorithm,[54,55] dubbed CirclePack, which we employ here. The procedure relies on recent developments in computational geometry,[56,57] in conjunction with the CirclePack procedure, which allows construction of quasiconformal maps in $\mathbb{H}^2$. We demonstrate its application *via* a number of examples with varying degrees of intrinsic hyperbolic symmetry, including symmetric TPMS and less symmetric related TP(M)S.

Consider first the map from a TPMS. We construct periodic triangulations of TPMS using the methods implemented in CGAL[56,57] *via* the ''nodal surface'' approximations of these surfaces.[58] (Notice that the mean curvature of these nodal surfaces is not zero, so these surfaces are strictly speaking TP(M)S, although they are virtually indistinguishable from their parent TPMS.) Each triangulated mesh is then input into CirclePack, yielding a quasi-conformal triangulated mesh in $\mathbb{H}^2$, which is aligned with the TP(M)S with the help of standard embeddings of the translational domains of these surfaces in $\mathbb{H}^2$.[17] The details of this process are outlined in the ESI.† The triangular meshes of the three TPMS in $\mathbb{E}^3$ and their corresponding meshes in $\mathbb{H}^2$ are shown in Fig. 2 along with decorations that will be relevant later.

Order in hyperbolic surfaces

Patterned curved surfaces embedded in usual three-space induce intrinsic symmetries within the two-dimensional surface as well as extrinsic symmetries, visible in three dimensions. For example, a patterned sphere in euclidean three-space induces intrinsic discrete isometries in the surface of the sphere and fixed-point isometries in three-space. The intrinsic order is captured by the spherical orbifold induced by the pattern, whereas its extrinsic order is associated with some point group. That distinction between intrinsic and extrinsic order is often overlooked in the

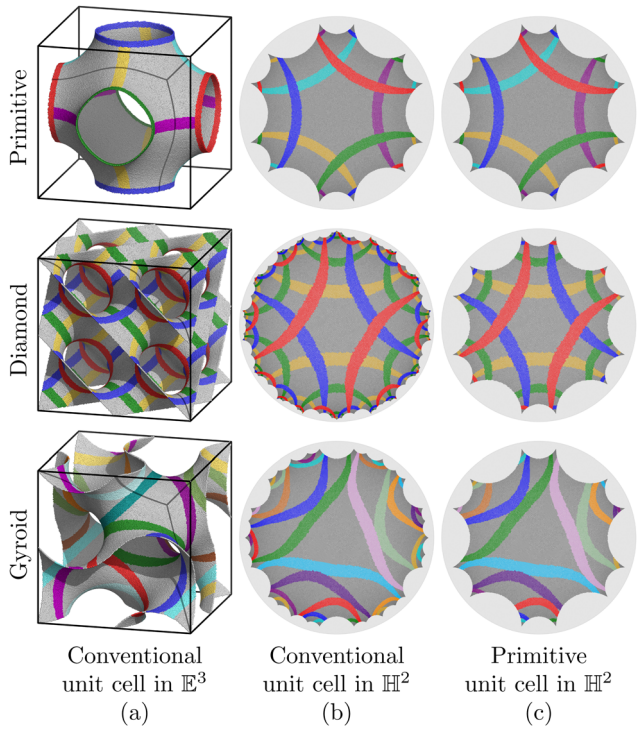

Fig. 2 (a) High-resolution triangulations of nodal approximations of the Primitive, Diamond and Gyroid TPMS[58] marked by colored collars (their shortest, non-trivial loops). Note that only half of the collars of the Gyroid are shown for simplicity. (b) Quasiconformal maps of the TPMS in $\mathbb{H}^2$, including the collars, colored as in (a). The maps are aligned with the translational domains of the surfaces given by their conventional cubic unit cells, corresponding to those shown in Fig. 1. (c) Dodecagonal regions excised from the maps in (b), corresponding to domains of ◦◦◦. Fig. S2 (ESI†) contains copies of these images with a grid of ⋆246 domains superimposed.

plane or on the sphere, since there is one-to-one correspondence between the planar or spherical isometries and wallpaper or point groups.[59] For example, an icosahedral pattern can be generated on the sphere by decorating a $\frac{\pi}{2},\frac{\pi}{3},\frac{\pi}{5}$ spherical triangle, followed by repeated reflections of that decorated triangle in its edges. That pattern has intrinsic order given by the orbifold symbol ⋆235 and extrinsic order given by the point group, labelled by the Schoenflies symbol I_h. Alternatively, a chiral icosahedral pattern results by repeated rotations of order 2, 3, 5 centred on vertices of the same triangle: that pattern has intrinsic order 235 and extrinsic order *I*. (Two-dimensional orbifolds are discussed further in the literature[59,60] and the ESI.†)

Patterned hyperbolic surfaces embedded in three-space also display intrinsic and extrinsic order. Again, their intrinsic order is described by the two-dimensional orbifold associated with the hyperbolic pattern. If the embedding of the hyperbolic surface is three-periodic its extrinsic order is described by the associated crystallographic space group. In the hyperbolic case orbifolds and space groups are not in one-to-one correspondence since TP(M)S can have different extrinsic embeddings.[59] The most symmetric pattern on a TPMS has orbifold symbol ⋆246,[48] in which case the asymmetric domain is defined by three mirror lines forming a hyperbolic triangle with vertex angles $\frac{\pi}{2},\frac{\pi}{4},\frac{\pi}{6}$. That intrinsic order is possible only in the Primitive, Gyroid and Diamond minimal surfaces, whereas less symmetric patterns can be found on other TP(M)S. Repeated rotations in the three vertices of that hyperbolic triangle (of order 2, 4, 6), with no reflections, generates a hyperbolic pattern with chiral intrinsic symmetry, denoted 246, analogous to chiral icosahedral patterns in the sphere. Since the variety and number of hyperbolic orbifolds far exceeds the more familiar spherical and flat orbifolds, it is useful to classify them into seven distinct classes, dependent on the topology of the orbifold, described elsewhere.[59] Those classes distinguish, for example, ''coxeter'' patterns (*e.g.* ⋆246, generated by mirrors alone) from ''stellate'' patterns (*e.g.* 246). Other orderings are possible, *e.g.* orbifolds containing only glide reflections or translations. Within each class, there is a unique, maximally symmetric, hyperbolic orbifold describing the intrinsic order of any hyperbolic film in three-space; each case can be realised by a patterned TPMS, as shown in the top row of Fig. 3.

Ordered patterns in a hyperbolic TP(M)S can be transformed to patterned Poincaré discs, *via* the algorithm introduced in the previous section. Since any hyperbolic isometry in the patterned TP(M)S induces the same isometry in its universal cover in $\mathbb{H}^2$, the intrinsic structural order within a triangulated mesh of the TP(M)S is retained in its corresponding mesh in $\mathbb{H}^2$, which in turn is retained in the final mesh in the flat disc, subject to the metric rescaling induced by the mapping from $\mathbb{H}^2$ to the Poincaré disc. (The metric rescaling is described in ESI.†) Despite that rescaling, the quasi-conformal nature of the map ensures that the final pattern retains all traces of intrinsic order in the original patterned TP(M)S. Careful inspection of a discretised disc map of a symmetrically patterned TP(M)S reveals the signatures of all of the intrinsic reflections, translations, *etc.*, modified by the inherent rescaling due to the Poincaré map.

To be more precise, the numerical implementation of our mapping algorithm necessarily introduces some disorder, due to discretisation. Nevertheless, the underlying order can be preserved modulo minor distortions, provided sufficient discs are introduced to the disc-packing algorithm. Consider for example a pattern on a true TPMS, such as the hyperbolic (low density) packing of warped ''pennies'' on the Primitive TPMS, shown in Fig. 1(b). That pattern results in a symmetric pattern in the unwrapped Poincaré model, shown in Fig. 1(c), provided the resolution includes many constituent discs in the discretisation of the penny pattern. Indeed, each disc is surrounded by six neighbours; their centres coincide with centres of 6-fold rotational symmetry, at which six mirror lines intersect. Those lines induce a pattern with ⋆246, characteristic of maximal symmetry on hyperbolic surfaces. Given that symmetry, we conclude the original penny pattern is ordered. Another example is afforded by mapping the so-called collars of the Primitive, Diamond, and Gyroid TPMS onto the Poincaré disc model. Recall that since these TPMS are not simply connected, some loops wrap around channels of the TPMS.

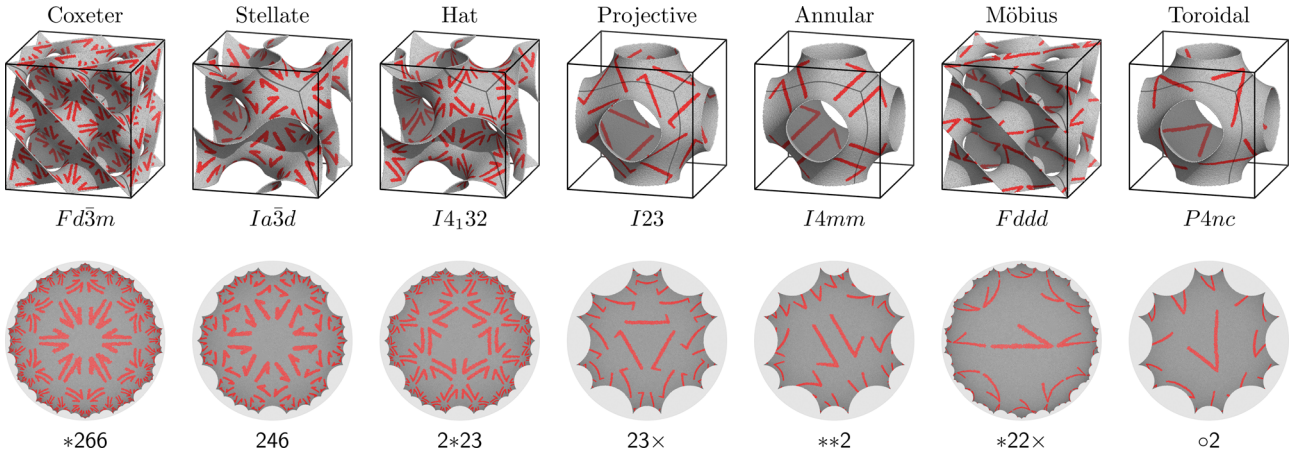

Fig. 3 Demonstration of maps of patterned TPMS to $\mathbb{H}^2$ for examples from each of the seven classes of orbifolds.[59] In the top row, we annotate each example by its space group, and below, by its corresponding orbifold symbol. Larger versions of the images in the bottom row with their asymmetric domains highlighted can be found in Fig. S3 (ESI†).

Those loops cannot be shrunk into a vanishingly small circuit in the surface. However, each such loop can be shrunk to a geodesic of shortest circumference; the simplest cases are the collars, which surround a single channel of the TPMS. Fig. 2 displays collars on all three TPMS and their images in the Poincaré model of $\mathbb{H}^2$ described above.

Thus, ordered patterns in TP(M)S induce characteristic maps in the Poincaré disc. With some practice, the intrinsic isometries of those maps – whether reflections, rotations, glide rotations or translations – can be detected by inspection, noting that translations traverse circular trajectories in the disc, leading to simultaneous rotation and shrinkage of motifs from the centre towards the disc edge. The discrete map therefore affords a useful insight into the degree of ordering in self-assemblies on TPMS or associated substrates, as we demonstrate below.

Examples

In our first examples, we analyse two very different systems confined to an *a priori* known surface, namely a TPMS. In those cases, we can analyse the emerging structures using the pre-computed meshes for the TPMS given in Fig. 2. Later, we explore assemblies leading to hyperbolic films whose geometry is unconstrained in two dimensions and relaxed in three-dimensional space. It is nevertheless, three-periodic since it is confined to a box with periodic boundary conditions. In that more general scenario, the mid-surface of the film is a TP(M)S, whose specific geometry is not known *a priori* and is not necessarily minimal.

Monte Carlo simulations of hard spheres on TPMS

In this section, we demonstrate the method applied to three examples of hard sphere packings on our TPMS published by Dotera *et al.*[61] as results of Monte Carlo simulations of hard spheres confined to the nodal approximation of these surfaces.[58] These structures realize the hyperbolic analogue of Caspar and Klug's hexagulation numbers;[62] we show an example from each of our surfaces in Fig. 4 produced using the reported crystallographic coordinates.[61] The patterns are readily visualized in $\mathbb{H}^2$ using the precomputed meshes from Fig. 2.

From the patterns visualized using the Poincaré disc, one readily identifies the in-surface symmetries described by two occurrences of the same hat orbifolds (4∗3) and a stellate orbifold (246) in these examples. We note that our visualization enables us to identify an intrinsic (*i.e.* in-surface) symmetry not realised as an extrinsic symmetry: *a priori* one would expect the space group $I\bar{4}3d$ to correspond to the orbifold symbol 344 on the Gyroid,[59] however, by considering the pattern in the

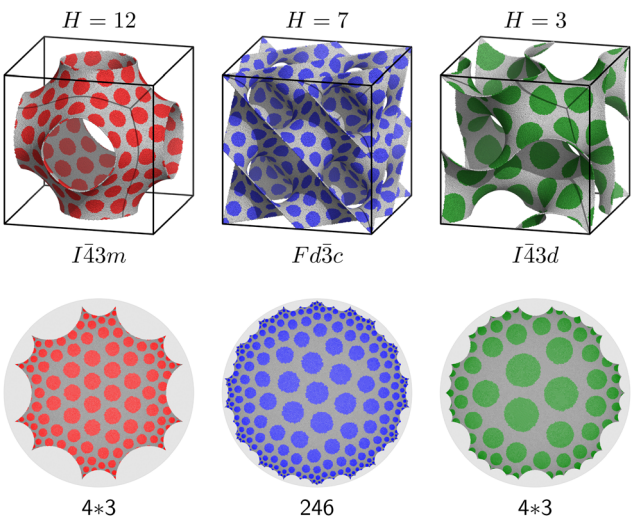

Fig. 4 Three examples of hard sphere packings on the TPMS enumerated by their hexagulations number, *H*. The translational domains contain 96, 224, and 48 particles/discs, respectively. The top row shows the surfaces inked by the crystallographic coordinates of the underlying structure along with the related space group. Below, we show the same structures visualized in $\mathbb{H}^2$ using the outlined methods along with their orbifold symbols. Versions of the images in the bottom row with the asymmetric domains/orbifolds annotated are available in the ESI.†

universal cover we identify that the in-surface symmetry is in fact an index-2 supersymmetry of 344, namely 4⋆3. The discrepancy emerges as the mirror symmetries in 4⋆3 are not realised as spatial symmetries in $\mathbb{E}^3$ *via* the embedding on the Gyroid.

Confined diblock co-polymer self-assembly

The examples above were unequivocally ordered, and their intrinsic symmetries are captured by analysis of the orbifolds in their patterned flat maps. We show next that less ordered patterns too can be fruitfully explored with this technique. The following examples explore numerical simulations of self-assemblies of diblock co-polymers, which are known to form intricate patterns resembling TPMS.[42] We first idealise those surface geometries numerically by confining the co-polymers to true TPMS and use our map to probe the evolution of hyperbolic order in time. Fig. 5(a–c) shows an example. The simulations explore the self-assembly of compositionally balanced diblock copolymers (an example of which is shown in Fig. 5(a)) confined to the Primitive surface using conventional dissipative particle dynamics (DPD) simulations.[64] Simulation details can be found in the ESI.† Simulation snapshots, plus their corresponding quasiconformal flat maps are shown in

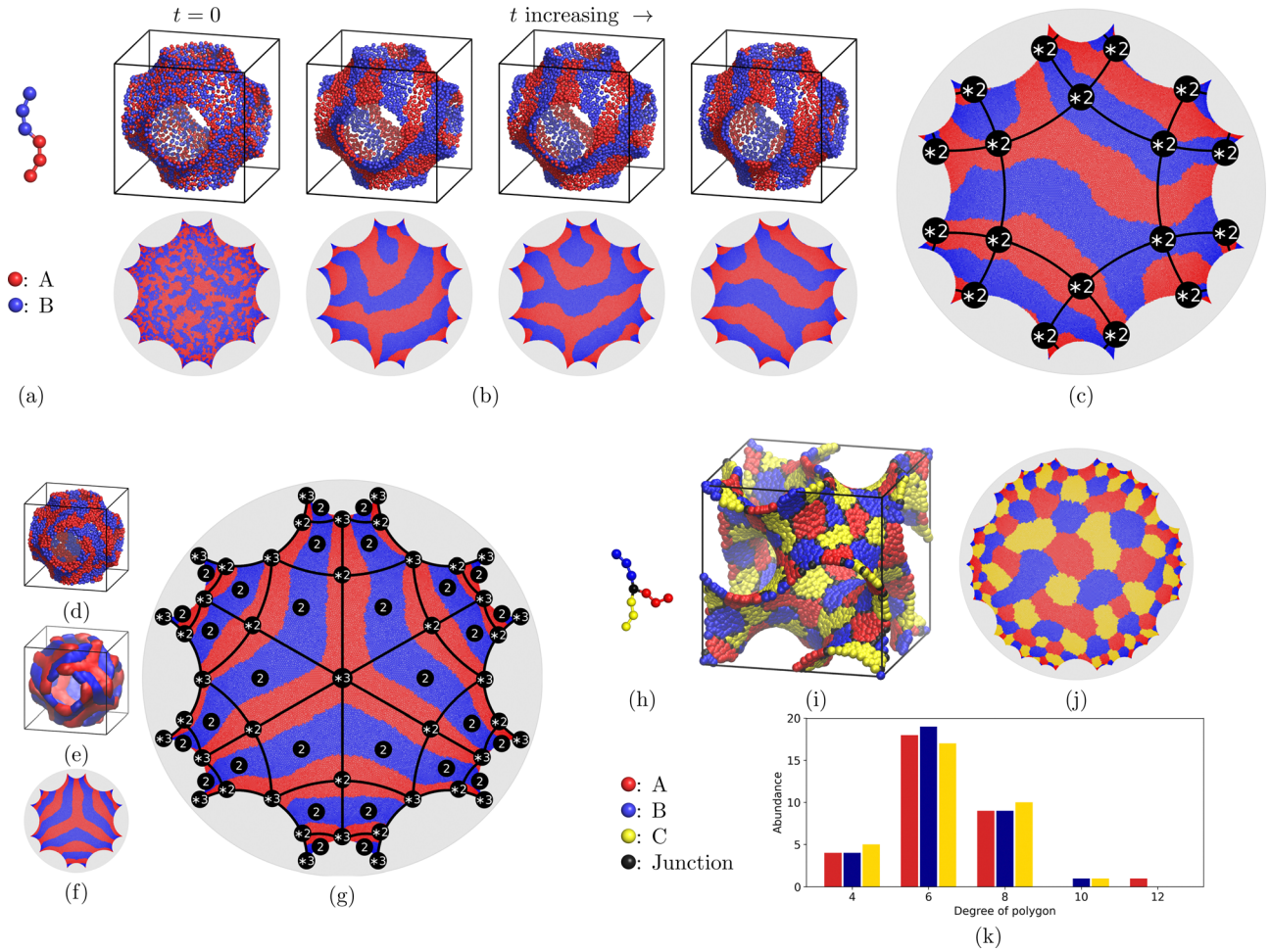

Fig. 5 Examples of confined DPD polymer simulations. See simulation details in the ESI.† (a–c) Time series of a DPD simulation of a 3 : 3 diblock co-polymer melt confined to the Primitive surface. (a) A single AB diblock molecule. (b) The upper row shows four snapshots of the self-assembly process of such molecules confined to the Primitive surface. The lower row shows corresponding quasiconformal maps in $\mathbb{H}^2$. (c) The final pattern, overlaid with a grid of ⋆222222 orbifolds. The black arcs are mirror lines and the black circles indicate the ⋆2 symmetry points. In Fig. S5 (ESI†), we demonstrate how rigid body transformations, which move different points to the center of the disc, enable the identification of mirror lines. (d–g) DPD simulation of 4 : 4 diblock co-polymers confined to the Primitive surface resulting in a hyperbolic forest structure. (d) A single snapshot of the simulation state after convergence. (e) Volumetric occupancy map over several frames in the simulation trajectory (after convergence). (f) The occupancy map in (e) visualized in $\mathbb{H}^2$ using the methods outlined in this paper. We note that the mesh is inked from the positions of the most occupied voxels in the volumetric occupancy map. (g) The intrinsic symmetries correspond to the orbifold 2⋆23 which signifies the pattern as the acosh(5) hyperbolic forest.[34,35,63] As in (c), the black lines are mirror lines, and the black circles denote either ⋆2 points, ⋆3 points, or rotational two-fold symmetries. (h–k) DPD simulation of a 3-armed star polymer confined to the Gyroid. (h) Rendering of a 3 : 3 : 3 ABC star polymer. (i) The final structure emerging in a DPD simulation of the polymers in (h) when confined to the Gyroid. (j) The structure from (i) visualized in $\mathbb{H}^2$ *via* the mesh introduced in Fig. 2. (k) Histogram of the abundance of the colored polygons in (j).

Fig. 5(b). The color coded polymer units phase separate, and over time we observe how the initial random configuration changes into locally phase separated ''colored'' domains.

The flat map affords a detailed portrayal of the evolution of the nanodomains in these copolymer assemblies over time: as the simulation progresses, domains merge and split, relaxing to form the structure in the final snapshot which is very nearly symmetric, as shown in Fig. 5(c). In fact, the pattern nearly exhibits ⋆222222 ($\star 2^6$) symmetry, *i.e.* subgroup #55 among the subgroups of ⋆246/∘∘∘.[16] That orbifold on the Primitive surface leads to a pattern with three-dimensional orthorhombic symmetry, corresponding to space group #47, or *Pmmm*.[59] The map in Fig. 5(c) also reveals that the red and blue domains are very nearly congruent: the center of an $\star 2^6$ patch (located at the origin of the Poincaré disc) hosts a site of two-fold rotational symmetry, which exchanges red and blue domains. Therefore the uncolored pattern, decorated only by the domain boundaries, has approximate symmetry 2⋆222 (subgroup #100), leading to a domain structure with three-dimensional orthorhombic symmetry *Immm*.[59] Clearly, the map offers insight into an otherwise extremely complex hyperbolic structure in $\mathbb{E}^3$. In fact, such detailed assignment of symmetries would be very difficult based on the 3D structure alone. We note in passing that the pattern found here is novel. Previous analyses of two-phase structures in TPMS have not explored structures with the approximate symmetries seen here[42] or the possibility of equivalent branched ribbon domains for both phases, observed here.[45]

Fig. 5(d–g) outlines the outcome of another such simulation of confined diblock co-polymers. Here, we observe the emergence of a pattern with approximate 2⋆23 symmetry (subgroup #129[16]) corresponding to space group #211, or *I*432.[59] This allows us to identify the pattern as the highly symmetric ''acosh(5) hyperbolic forest''[34,35,63] previously hypothesised to form on the Gyroid, but not found.[42] We note that while the pattern in Fig. 5(c) includes an approximate isometry which exchanges red and blue domains, the pattern in Fig. 5(f and g) demonstrates spontaneous symmetry breaking in the system; despite identical ''molecular'' interactions and structure, the red and blue ribbon structures are not related *via* symmetry.

Confined triblock co-polymer self-assembly

The simulations described in the previous section are readily extended to molecules with a more elaborate architecture. Here too, the discrete map affords useful structural insights. Fig. 5(h–k) shows the outcome of a DPD simulation of three-armed star polymers confined to the Gyroid. As above, all arms are equal, ensuring that each color fills the same volume. The resulting pattern is analogous to those formed by self-assembly of balanced 3-arm stars in the flat plane, which form a 3-colored hexagonal tiling.[66] A single simulation of the hyperbolic assembly gives the map in Fig. 5(j), which reveals nanodomains, forming a somewhat disordered tessellation of the Gyroid by hyperbolic polygons, whose topologies are easily interpreted from the disc image. We note that the boundary arcs of domains merge at trivalent vertices, subtending angles close to $\frac{2\pi}{3}$, as in the planar analogue. Each domain is an even-sided polygon, allowing alternating coloring of the surrounding polygons, thereby ensuring three-coloring of all vertices. We have collected statistics for the number of sides (degree) of all polygons in Fig. 5(j), giving the distributions in Fig. 5(k). As expected, all three colours give similar polygon statistics, leading to an average polygon degree of 6.5.

Those statistics imply a preferred extension of the copolymer arms, which can be estimated as follows. We simplify the polygons, and model them as symmetric n-gons with equal sides and equal internal vertex angles of $\frac{2\pi}{3}$. Standard formulae for regular polygons in $\mathbb{H}^2$ give in- and out-radii of:

$$\rho_{\text{in}} = \operatorname{acosh}\left(\frac{\operatorname{cosec}\left(\frac{\pi}{n}\right)}{2}\right) \quad \rho_{\text{out}} = \operatorname{acosh}\left(\frac{\cot\left(\frac{\pi}{n}\right)}{\sqrt{3}}\right)$$

or an average radius of approximately 0.41, estimated by averaging in- and out-radii and setting n = 6.5. That radius needs to be rescaled, since $\mathbb{H}^2$ has unit radius of curvature, whereas the Gyroid in the simulation has a (surface-averaged value of) the radius of curvature equal to:[67]

$$\bar{\rho} = \left(\frac{\mathscr{H}}{-2\pi\chi}\right)^{\frac{1}{3}} L$$

Here, L is the lattice parameter of the simulation box, $2\pi\chi$ is the integral (Gaussian) curvature of the Gyroid within the box and $\mathscr{H}$ is the dimensionless surface-to-volume ratio of the Gyroid. Since the simulation assigns a unit distance between relaxed beads and confines the Gyroid to a cube of edge-length 20, L = 20, χ = −8 and $\mathscr{H}$ = 0.7665, so its average radius of curvature is $\bar{\rho}$ = 4.96. Therefore the extension of each arm in the star copolymer has an average value of approximately 0.41 × 4.96. That implies that each arm, whose relaxed end-to-end distance is at most 3, optimises its chain entropy by forming chains whose end-to-end distance is approximately 2.1. In other words, an estimate of the average value of the relaxed arm length in the copolymer assembly can be deduced from the average polygon size of 6.5, which is easily detected in the map shown in Fig. 5(j).

Unconfined co-polymer self-assembly in three-dimensions

The previous examples demonstrate self-assembly of polymers under confinement. In this section we turn our attention to bulk self-assembly. This case is different from those above, since we no longer assume the structure forms on a predetermined surface. Here the surface emerges from the simulations, and is found numerically using the method outlined in the ESI.† We note that the only requirement here is that the surface is a TP(M)S, sufficiently well sampled that the topology of the resulting mesh is that of a TP(M)S. Earlier three-dimensional simulations of star polymers have revealed the gradual assembly of complex ribbon-shaped domains within a TP(M)S resembling the Gyroid.[42]

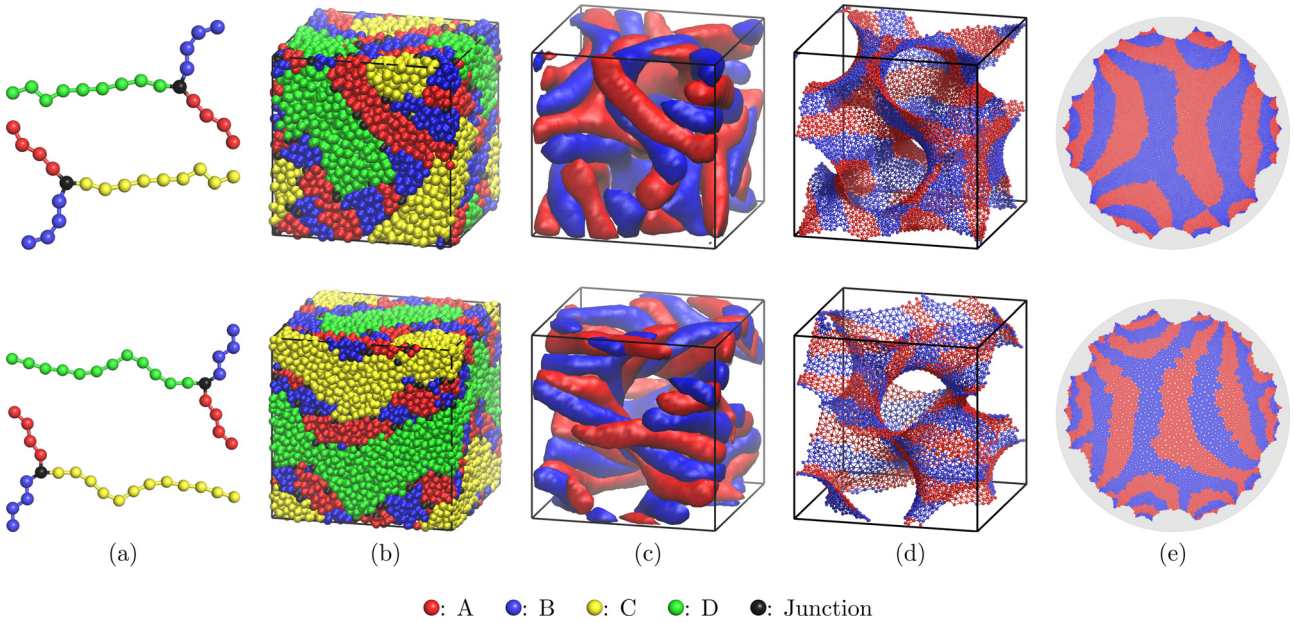

Fig. 6 The pipeline affords an explicit view of hyperbolic patterns in bulk star polymer assemblies. (Details of these simulations and the emergence of Gyroid-like phases are explained elsewhere.[42]) (a) Renderings of models of ABC- and ABD-miktoarm star polymers emphasizing their molecular architecture, with relative molecular weights of 4 : 4 : 9 and 4 : 4 : 12, respectively. The color scheme is explained in the bottom of the figure. (b) Two examples of the final frame of DPD molecular dynamics simulations of a 1 : 1 mixture of the molecules in (a). (c) Volumetric occupancy maps[65] of the two minority components, A and B, of the simulated polymers averaged over the last several frames in the trajectories – exhibiting a morphology reminiscent of the Gyroid surface. (d) Triangular, periodic meshes refined from the structures in (c). Edges connecting vertices near the boundary of our unit cell to vertices on the opposing boundary are not shown. (e) The meshes in (d) visualized in $\mathbb{H}^2$. The geodesics used for the alignment process (as explained in Fig. S1) can be found in the ESI.†

The self-assembly of those star polymers was simulated by filling a periodic cube with a 1 : 1 mixture of the star polymers shown in Fig. 6(a), then computing the equilibrium structure of the polymer mixture *via* DPD, giving assemblies such as those in Fig. 6(b). These three-dimensional data allowed us to construct surface maps as shown in Fig. 6(c). First, we selected the two minority components of our polymer molecules for further analysis and computed the volumetric occupancy maps[65] of the two components. From these, we refined a periodic mesh representing the underlying TP(M)S using the methods outlined above. The resulting mesh is shown in Fig. 6(d). Lastly, we computed the quasiconformal flat map shown in Fig. 6(e).

The maps give useful insights into these assemblies, Fig. 6 shows two such phases and their discrete flat maps. The domain patterns, including their in-surface connectivity and approximate symmetry, as well as a variety of other structural, geometric, and topological properties are readily identified from the quasiconformal maps. For example, the upper and lower maps in Fig. 6(e) reveal striking differences in the in-surface widths of the (blue) ribbon domains: the upper map contains thicker ribbons than the lower, accompanied by less branching. Such information is physically significant, yet very difficult to extract from a conventional three-dimensional surface visualisation.

Discussion and conclusions

We have presented a computational pipeline for analysis and visualization of patterns which form on surfaces of negative Gaussian curvature in the flat plane, *via* flat maps induced by their universal cover, the hyperbolic plane, $\mathbb{H}^2$. We note that our map necessarily smoothes out all variations of Gaussian curvature, essentially moulding the TP(M)S to the hyperbolic plane, which has constant Gaussian curvature. However, smoothing does not remove any intrinsic order in the original patterned hyperbolic surface, assumed here to be a TP(M)S. After all, the pattern cannot be more intrinsically symmetric than that of the underlying surface, which in turn is set by the variations of Gaussian curvature in the surface (*e.g.* *246 for the TPMS, *2223 for the TP(M)S parallel to the Primitive TPMS). Thus, the map retains the intrinsic order of its inhomogenous TP(M)S precursor.

We have explored two scenarios. The first assumes the structure is localised on a fixed surface of prescribed geometry, namely a TPMS. The second demands only an arbitrary TP(M)S. The simulation gives a thickened connected film, whose mid-surface is constrained only to be three-periodic.

The first scenario allows analysis of idealized cases where particles, patterns, or impurities, *etc.* are confined to a surface of specified geometry, namely the three simpler TPMS. However, the pipeline can be readily extended to other surfaces whose hyperbolic crystallography is established.[59] Those surfaces include the two-periodic (genus-2) HCB- and SQL-surfaces,[36,68] as well as other TPMS, such as the (genus-3) H-surface[12] with hexagonal symmetry, the (genus-3) CLP-surface[12] and the (genus-4) I-WP-surface;[13] all of which are relevant to microstructured materials. We have analysed data from Dotera *et al.* of hard sphere arrays confined to TPMS, as well as our own

simulations of confined co-polymers. Other systems are relevant to the simpler confinement scenario. We mention in particular recent work exploring the dynamics of active matter confined to TPMS,[69] zeolites templated on TPMS[25] and self-assembly of colloids forming surfaces of negative curvature.[70,71] The second scenario is broader still, since it does not impose a specific surface geometry. Rather, any hyperbolic TP(M)S (in the sense defined in ESI†) can be analysed, giving a simple planar representation of patterning in these otherwise topologically complex convoluted surfaces. The technique allows us to identify the underlying ideal order in a patterned hyperbolic film, such as the examples in Fig. 5(c, g and j). Armed with that ideal, defect-free, pattern, defects in the actual film can be readily detected and characterised.

In summary, the numerical pipeline and analysis of the topologies and symmetries of these maps afford a practical insight into self-assemblies of multiple species within a three-periodic hyperbolic film, giving multi-coloured hyperbolic patterns. While we have focused here on simulations, the same technique can be applied to experimental data. Due to recent advances in nanoscale imaging techniques, experimental evidence of intrinsic hyperbolic patterning has become increasingly obtainable in recent years.[72,73]

Software

The initial handling, smoothing, and generation of the periodic meshes needed as input to the disc packing algorithm were handled using CGAL.[57] Further handling of the meshes was done using the OpenMesh Python module. The molecular dynamics simulations were performed using HooMD-blue[74,75] based on the DPD model.[64] Visualizations of the patterns on the Poincaré disc were done using the Python module Matplotlib, and the three-dimensional graphics were rendered using Pymol, VMD, and SideFX Houdini.

Our Python code for constructing, manipulating, and visualizing hyperbolic patterns represented in the Poincaré disc model of $\mathbb{H}^2$ is available *via* the Gitlab repository at **https://www.gitlab.com/mcpe/H2Tools**. Examples and scripts are available from the same repository. Scripts for handling points set and meshes in C++ and CGAL are also available from this repository.

Conflicts of interest

The authors have no conflicts of interest to declare.

Acknowledgements

The authors thank V. Robins, O. Delgado-Friedrichs, A. Dahl, and M. Teillaud for discussions and feedback. The Villum Foundation is gratefully acknowledged by MCP for financial support *via* grant 22833.

References

1 J. J. Thomson, *Philos. Mag. J. Sci.*, 1904, **7**, 237–265.
2 S. B. Rochal, O. V. Konevtsova, A. E. Myasnikova and V. L. Lorman, *Nanoscale*, 2016, **8**, 16976–16988.
3 P. Lipowsky, M. J. Bowick, J. H. Meinke, D. R. Nelson and A. Bausch, *Nat. Mater.*, 2005, **4**, 407–411.
4 M. J. W. Dodgson and M. A. Moore, *Phys. Rev. B: Condens. Matter Mater. Phys.*, 1997, **55**, 3816.
5 T. Hain, G. E. Schroeder-Turk and J. J. K. Kirkensgaard, *Soft Matter*, 2019, **15**, 9394–9404.
6 D. J. Wales, H. McKay and E. L. Altschuler, *Phys. Rev. B: Condens. Matter Mater. Phys.*, 2009, **79**, 224115.
7 W. Irvine, V. Vitelli and P. Chaikin, *Nature*, 2010, **468**, 947–951.
8 W. Irvine and V. Vitelli, *Soft Matter*, 2012, **8**, 10123–10129.
9 V. Schmid and A. Voigt, *Soft Matter*, 2014, **10**, 4694–4699.
10 N. A. Garca, R. A. Register, D. A. Vega and L. R. Gómez, *Phys. Rev. E: Stat., Nonlinear, Soft Matter Phys.*, 2013, **88**, 012306.
11 H. Kusumaatmaja and D. Wales, *Phys. Rev. E: Stat., Nonlinear, Soft Matter Phys.*, 2013, **110**, 165502.
12 H. A. Schwarz, *Gesammelte mathematische Abhandlungen*, 1890.
13 A. Schoen, *Infinite periodic minimal surfaces without self-intersections*, NASA, 1970.
14 V. Castelletto and I. Hamley, *Curr. Opin. Solid State Mater. Sci.*, 2004, **8**, 426–438.
15 R. Mezzenga, J. Seddon, C. Drummond, B. Boyd, G. Schröder-Turk and L. Sagalowicz, *Adv. Mater.*, 2019, **31**, 1900818.
16 V. Robins, S. J. Ramsden and S. T. Hyde, *Eur. Phys. J. B*, 2004, **39**, 365–375.
17 M. C. Pedersen, V. Robins and S. T. Hyde, *Acta Crystallogr., Sect. A: Found. Adv.*, 2022, **78**(1), 56–58.
18 P. Mariani, V. Luzzati and H. Delacroix, *J. Mol. Biol.*, 1988, **204**, 165–189.
19 H. Delacroix, T. Gulik-Krzywicki, P. Mariani and V. Luzzati, *J. Mol. Biol.*, 1993, **229**, 526–539.
20 T. Oka, N. Ohta and S. T. Hyde, *Langmuir*, 2018, **34**, 15462–15469.
21 T. Oka, N. Ohta and S. T. Hyde, *Langmuir*, 2020, **36**, 8687–8694.
22 J. Dolan, B. Wilts, S. Vignolini, J. Baumberg, U. Steiner and T. Wilkinson, *Adv. Opt. Mater.*, 2015, **3**, 12–32.
23 Z. Almsherqi, S. Kohlwein and Y. Deng, *J. Cell Biol.*, 2006, **173**, 839–844.
24 K. Nakazato, K. Oyamatsu and S. Yamada, *Phys. Rev. Lett.*, 2009, **103**, 132501.
25 E. Braun, Y. Lee, S. Moosavi, S. Barthel, R. Mercado, I. Baburin, D. Proserpio and B. Smit, *Proc. Natl. Acad. Sci. U. S. A.*, 2018, **115**, E8116–E8124.
26 A. Mackay and H. Terrones, *Nature*, 1991, **352**, 762.
27 N. Park, M. Yoon, S. Berber, J. Ihm, E. Osawa and D. Tomanek, *Phys. Rev. Lett.*, 2003, **91**, 237204.
28 A. V. Rode, E. G. Gamaly, A. Christy, J. F. Gerald, S. Hyde, R. Elliman, B. Luther-Davies, A. Veinger, J. Androulakis and J. Giapintzakis, *Phys. Rev. B: Condens. Matter Mater. Phys.*, 2004, **70**, 054407.

29 J. Llandro, D. Love, A. Kovács, J. Caron, K. Vyas, A. Kákay, R. Salikhov, K. Lenz, J. Fassbender, M. Scherer, C. Cimorra, U. Steiner, C. H. W. Barnes, R. Dunin-Borkowski, S. Fukami and H. Ohno, *Nano Lett.*, 2020, **20**, 3642–3650.
30 S. Robbins, P. Beaucage, H. Sai, K. Tan, J. Werner, J. Sethna, F. DiSalvo, S. Gruner, R. V. Dover and U. Wiesner, *Sci. Adv.*, 2016, **2**, 1501119.
31 J. Sadoc and J. Charvolin, *Acta Crystallogr., Sect. A: Found. Crystallogr.*, 1989, **45**, 10–20.
32 M. O'Keeffe, M. A. Peskov, S. J. Ramsden and O. M. Yaghi, *Acc. Chem. Res.*, 2008, **41**, 1782–1789.
33 S. J. Ramsden, V. Robins and S. T. Hyde, *Acta Crystallogr., Sect. A: Found. Crystallogr.*, 2009, **65**, 81–108.
34 M. E. Evans, V. Robins and S. T. Hyde, *Acta Crystallogr., Sect. A: Found. Crystallogr.*, 2013, **69**, 241–261.
35 M. E. Evans, V. Robins and S. T. Hyde, *Acta Crystallogr., Sect. A: Found. Crystallogr.*, 2013, **69**, 262–275.
36 M. C. Pedersen and S. T. Hyde, *Acta Crystallogr., Sect. A: Found. Adv.*, 2017, **73**, 124–134.
37 M. C. Pedersen and S. T. Hyde, *Proc. Natl. Acad. Sci. U. S. A*, 2018, **115**, 6905–6910.
38 M. C. Pedersen, O. Delgado-Friedrichs and S. T. Hyde, *Acta Crystallogr., Sect. A: Found. Adv.*, 2018, **74**, 223–232.
39 B. Kolbe and M. E. Evans, *SIAM J. Appl. Algebra Geom.*, 2022, **6**, 1–40.
40 B. Kolbe and M. E. Evans, *Geom. Dedicata*, 2021, **212**, 177–204.
41 S. T. Hyde and M. C. Pedersen, *Proc. Roy. Soc. A*, 2021, **477**, 20200372.
42 J. J. K. Kirkensgaard, M. E. Evans, L. de Campo and S. T. Hyde, *Proc. Natl. Acad. Sci. U. S. A*, 2014, **111**, 1271–1276.
43 B. Kolbe and V. Robins, in *Research in Computational Topology 2*, ed. E. Gasparovic, V. Robins and K. Turner, Springer, Cham, Switzerland, 2022, pp. 77–98.
44 J. J. K. Kirkensgaard, *Interface Focus*, 2012, **2**, 602–607.
45 L. De Campo, T. Castle and S. T. Hyde, *Interface Focus*, 2017, **7**, 20160130.
46 W. P. Thurston, *The Geometry and Topology of Three-Manifolds*, Princeton University, Princeton, 1980.
47 J. H. Conway, H. Burgiel and C. Goodman-Strauss, *The Symmetries of Things*, CRC Press, Wellesley, Massachusets, 2008.
48 S. Bai, V. Robins, C. Wang and S. Wang, *Geom. Dedicata*, 2017, **189**, 79–95.
49 A. Fogden and S. T. Hyde, *Acta Crystallogr., Sect. A: Found. Crystallogr.*, 1992, **48**, 442–451.
50 A. Fogden and S. T. Hyde, *Acta Crystallogr., Sect. A: Found. Crystallogr.*, 1992, **48**, 575–591.
51 V. Robins, S. J. Ramsden and S. T. Hyde, *Eur. Phys. J. B*, 2005, **48**, 107–111.
52 C. F. Gauss, *Disquisitiones generales circa superficies curvas*, Typis Dieterichianis, 1828.
53 T. A. Driscoll and L. N. Trefethen, *Schwarz-Christoffel Mapping*, Cambridge University Press, 2002.
54 T. Dubejko and K. Stephenson, *Exp. Math.*, 1995, **4**, 307–348.
55 C. R. Collins and K. Stephenson, *Comput. Geom.*, 2003, **25**, 233–256.
56 A. Pellé and M. Teillaud, Periodic meshes for the CGAL library, 23rd International Meshing Roundtable (IMR23), 2014.
57 The CGAL Project, CGAL–The Computational Geometry Algorithms Library, 2022, **https://www.cgal.org**.
58 H. G. von Schnering and R. Nesper, *Z. Phys. B*, 1991, **83**, 407–412.
59 S. T. Hyde, S. J. Ramsden and V. Robins, *Acta Crystallogr., Sect. A: Found. Adv.*, 2014, **70**, 319–337.
60 J. H. Conway and D. H. Huson, *Struct. Chem.*, 2002, **13**, 247–257.
61 T. Dotera, H. Tanaka and Y. Takahashi, *Struct. Chem.*, 2017, **28**, 105–112.
62 D. L. Caspar and A. Klug, Physical principles in the construction of regular viruses, *Cold Spring Harbor symposia on quantitative biology*, Cold Spring Harbor Laboratory Press, 1962, vol. 27, pp. 1–24.
63 S. Hyde and C. Oguey, *Eur. Phys. J. B*, 2000, **630**, 613–630.
64 C. L. Phillips, J. A. Anderson and S. C. Glotzer, *J. Comput. Phys.*, 2011, **230**, 7191–7201.
65 W. Humphrey, A. Dalke and K. Schulten, *J. Mol. Graphics*, 1996, **14**, 33–38.
66 J. J. K. Kirkensgaard, M. C. Pedersen and S. T. Hyde, *Soft Matter*, 2014, **10**, 7182–7194.
67 S. T. Hyde, *Curr. Opin. Solid State Mater. Sci.*, 1996, **1**, 653–662.
68 V. Luzzati, A. Tardieu and T. Gulik-Krzywicki, *Nature*, 1968, **217**, 1028–1030.
69 P. W. A. Schönhöfer and S. C. Glotzer, Curvature-Controlled Geometrical Lensing Behavior in Self-Propelled Colloidal Particle Systems, 2022, **https://arxiv.org/abs/2202.09713**.
70 P. W. A. Schönhöfer, M. Marechal, D. J. Cleaver and G. E. Schröder-Turk, *J. Chem. Phys.*, 2020, **153**, 034903.
71 P. W. A. Schönhöfer, M. Marechal, D. J. Cleaver and G. E. Schröder-Turk, *J. Chem. Phys.*, 2020, **153**, 034903.
72 X. Feng, C. J. Burke, M. Zhuo, H. Guo, K. Yang, A. Reddy, I. Prasad, R. M. Ho, A. Avgeropoulos, G. M. Grason and E. L. Thomas, *Nature*, 2019, **575**, 175–179.
73 X. Feng, M. Zhuo, H. Guo and E. L. Thomas, *Proc. Natl. Acad. Sci. U. S. A*, 2021, **118**, 1–6.
74 J. A. Anderson, C. D. Lorenz and A. Travesset, *J. Comput. Phys.*, 2008, **227**, 5342–5359.
75 J. Glaser, T. D. Nguyen, J. A. Anderson, P. Lui, F. Spiga, J. A. Millan, D. C. Morse and S. C. Glotzer, *Comput. Phys. Commun.*, 2015, **192**, 97–107.

